Direct magnetic manipulation of a Permalloy nanostructure by a focused cobalt-ion beam

Javier Pablo-Navarro,[1] Nico Klingner,[1] Gregor Hlawacek,[1] Attila Kákay,[1] Lothar Bischoff,[1] Ryszard Narkowicz,[1] Paul Mazarov,[2] René Hübner,[1] Fabian Meyer,[2] Wolfgang Pilz,[2] Jürgen Lindner,[1] and Kilian Lenz[1,*]

[1] *Helmholtz-Zentrum Dresden-Rossendorf, Institute of Ion Beam Physics and Materials Research, Bautzner Landstraße 400, Dresden 01328, Germany*

[2] *Raith GmbH, Konrad-Adenauer-Allee 8, Dortmund 44263, Germany*

(Received 25 April 2023; revised 14 September 2023; accepted 2 October 2023; published 26 October 2023)

We present results of direct maskless magnetic patterning of ferromagnetic nanostructures using a cobalt focused-ion-beam (FIB) system. The liquid-metal ion source of the FIB was made of a $Co_{36}Nd_{64}$ alloy. A Wien mass filter allows the ion species to be selected. Using the FIB, we implanted narrow tracks of Co ions into a nominal $5000 \times 1100 \times 53$ nm^3 Permalloy strip. We observed the Co-induced changes of the magnetic properties by measuring the sample with microresonator ferromagnetic resonance before and after the implantation. Regions as small as 40 nm can be implanted up to concentrations of 10 at % near the surface. This allows for easy magnetic modification of edge-localized spin waves with a lateral resolution otherwise hard to reach. The direct-write maskless FIB process is quick and convenient for optical measurement techniques, as it does not involve the virtually impossible removal of the ion-hardened resist masks one would face when using lithography with broad-beam ion implantation.

DOI: 10.1103/PhysRevApplied.20.044068

I. INTRODUCTION

Magnetic nanostructures are the essential ingredients of future spintronic devices. Strikingly, such building blocks currently pave the way to novel concepts for neuromorphic computing [1–4]. From the nanofabrication perspective, these nanostructures are usually defined by optical lithography techniques using resist masks with subsequent ion etching or lift-off processes. Nevertheless, such resist masks can also be employed for local ion-beam implantation to control the magnetic properties of the building blocks, like saturation magnetization, magnetic anisotropy, interlayer exchange coupling, or damping of the ferromagnetic material locally; see e.g. Refs. [5,6] and references therein. Unfortunately, the ion bombardment hardens the resist of the protected areas such that it is almost impossible to completely remove all traces of the baked resist afterwards. This might pose a problem for optical measurement techniques like Brillouin-light scattering or magneto-optical Kerr effect. In order to overcome this kind of problem, a direct-write (maskless) magnetic modification technique is beneficial.

For this purpose, using a focused ion beam (FIB) is a suitable alternative. It offers a very high lateral resolution down to the nanometer range and an exceptional flexibility in terms of pattern adaptation, which is hard to achieve using research-grade lithography processes. Even though FIB implantation and FIB prototyping of nanostructures is a well-known and widely used technique [7], the quasi-industry-standard for FIB sources is Ga. Harnessing the potential of ion implantation, a few groups worldwide still develop liquid-metal ion sources (LMISs) from other pure metals or liquid-metal-alloy ion sources (LMAISs) (see Refs. [8–10] for reviews). Among the variety of available elements, it is worth mentioning that focused ion beams of rare-earth elements (e.g., Y, Ce, Er, or Pr) have been used for applications to modify optical crystals for qubits [11–14].

So far, however, there have not been many studies regarding magnetic ions, so that further research still remains to be done. For instance, Mn^+ ions provided by a MnAs source were used to locally modify GaAs semiconductors [15]. Focused Co-ion beams can be applied to locally change the interlayer exchange coupling in $Ni_{81}Fe_{19}/Ru/Co_{90}Fe_{10}$ trilayer films from antiferromagnetic to ferromagnetic coupling [16]. Interestingly, the use of Ni-ion implantation does not only induce interfacial mixing of $Ni_{81}Fe_{19}/Ta$ bilayers [17], but also allows tailoring the saturation magnetization, magnetic anisotropy, and damping parameter values of $Ni_{81}Fe_{19}$ films [18].

In this work, we report on the use of $Co_{36}Nd_{64}$ LMAIS [8,19,20] to locally tune the magnetic properties in

*k.lenz@hzdr.de

specific parts of a micrometer-sized Permalloy ($Ni_{80}Fe_{20} \equiv$ Py) strip by Co^{2+} implantation. We track the Co-induced changes of the magnetization dynamics by microresonator ferromagnetic resonance (FMR) [21–26] before and after each preparation step.

II. EXPERIMENTAL DETAILS AND SAMPLE PREPARATION

A. Sample preparation

The experiments were performed on two single ferromagnetic Py strips, each prepared into the loop of a planar microresonator structure [21,22]. First, the microresonator structure with a nominal loop diameter of 10 μm was prepared by photolithography, molecular-beam epitaxy, and subsequent lift-off on a high-resistivity Si(001) substrate [21–23]. The metallization of the microresonator layout as well as the backside metallization each consist of Cr(5 nm)/Cu(600 nm)/Au(100 nm). The microresonator structure was designed and optimized for a resonant frequency of around 14 GHz and 50 Ω impedance using the electromagnetic wave simulation package HFSS from Ansys [21,22]. The Py strip with nominal dimensions of $5000 \times 1100 \times 53$ nm^3 was patterned into the center of the microresonator loop by electron-beam lithography, Py evaporation, and subsequent lift-off. Figure 1(a) shows the Py strip inside the microresonator loop. In addition, five Py thin-film reference samples with the same thickness were prepared.

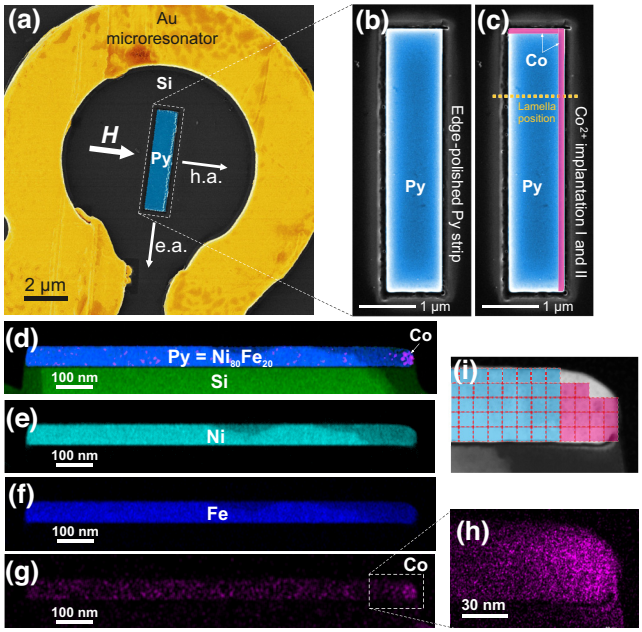

FIG. 1. (a) False-color SEM top-view image of the edge-polished Py strip sample inside the microresonator loop. Labels "e.a." and "h.a." denote the easy and hard axis of magnetization, respectively. (b),(c) SEM top-view images, with the Co-implanted areas marked in purple. The dashed line in panel (c) marks the position from which the TEM lamella was taken. (d)–(h) Chemical maps of the Co-implanted strip showing the spatial distribution of Ni (cyan), Fe (blue), Co (purple), and Si (green). (i) Sketch of the mesh used in the MUMAX^3 simulations: blue cells denote Permalloy parameters and purple cells Co-implanted Permalloy parameters.

B. Ne focused-ion-beam trimming

The shape of the sample after the lithographic preparation of the strip usually is not perfect. The sides might not be fully straight, or roughness and jitter on the long edges are visible. This eventually causes the edge mode resonance to vanish. To acquire a nearly perfect rectangular sample shape and optimized low roughness of the Py strips' side walls, the side walls have been trimmed by a focused Ne-ion beam using a Carl Zeiss ORION NanoFab helium-ion microscope system. The Ne^+ ion energy was set to 25 keV. Each side was trimmed by a few nanometers using one or more coarse cuts in a double-serpentine motion followed by one polishing step in a line mode. The beam current was set to 2.2 pA with a Ne^+ fluence of 5×10^{17} ions/cm^2 and a pixel spacing of 0.5 nm for both the coarse and polishing cuts. Figures 1(a) and 1(b) show false-color top-view scanning electron microscopy (SEM) images, acquired after all four sides were trimmed using the focused Ne^+ ion beam. Thus, the final size of the strip became $4840 \times 1035 \times 53$ nm^3. The optimized sample shape also facilitates modeling the sample for micromagnetic simulations.

C. Focused-ion-beam implantation using Co^{2+} ions

For the FIB implantation of the Co ions into the Py strip, we used the VELION FIB/SEM dual-beam system from Raith [27], which is equipped with a mass-separating column. The column offers acceleration voltages up to 35 kV, allowing ion energies up to 70 keV for doubly charged species. An $E \times B$ Wien filter in combination with the custom-built LMAIS provides for rapid selection and changing of the ion species for the FIB—different from the standard single-element (e.g., Ga) sources [9,28,29]. For this work, we used the alloy $Co_{36}Nd_{64}$. This LMAIS was developed and investigated already in the past [19,20], and used, for example, for the fabrication of $CoSi_2$ nanostructures on a Si surface [30].

We performed simulations of the Co-ion implantation process using the TRIDYN software [31]. This is a prerequisite for two reasons: (i) to select a proper kinetic ion energy, which sets the stopping range of the ions (i.e., the penetration depth)—this is important to avoid intermixing with the substrate; and (ii) to select a proper fluence, where, on the one hand, surface sputter effects are still small but,

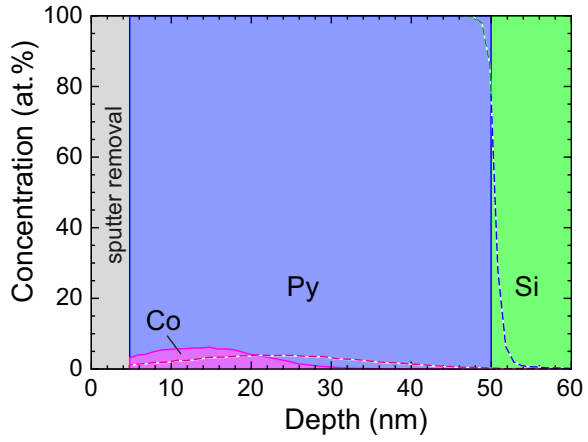

FIG. 2. TRIDYN simulation of the implantation profile (atomic concentration) of a 50-nm-thick Py film using a Co-ion fluence of 1.0×16 ions/cm^2 and a kinetic energy of 35 keV. The concentrations of Fe and Ni are displayed as a sum to represent the Permalloy layer. Dashed lines correspond to the distribution calculated for 70 keV. Depth zero corresponds to the surface of the as-grown sample, whereas implantation removes (sputter effect) the first 4.7 nm of the sample (grey area).

on the other hand, enough ions are implanted to have a magnetic effect.

Figure 2 shows the simulated depth profile of the atomic concentrations of Py, Co, and Si for a Co-ion fluence of 1.0×10^{16} ions/cm^2 and kinetic energies of 35 keV (filled areas) and 70 keV (dashed lines), respectively. At 35 keV the Co ions stop within the first 20 nm of Py, whereas at 70 keV they penetrate a bit deeper and a slight intermixing of ± 5 nm at the Py–Si interface occurs as shown by the dashed line in Fig. 2. At the given fluence, the ions already have a sputter effect on the surface, i.e., almost 5 nm of the Py surface is sputtered away (grey area). At higher fluences, like 5.0×10^{16} ions/cm^2, the initial film thickness of 50 nm would be sputtered even further down to 36.4 nm (not shown).

The Py strips were implanted using focused Co^{2+} ions along two consecutive edges of the strip, as illustrated in Figure 1(c). Thus, the strip exhibits both implanted and unimplanted long and short edges, respectively. The unimplanted edges serve as references in the FMR spectra. Upon ion implantation of *one* of the edges, the corresponding edge mode should be magnetically modified and change its resonance field position, whereas the response of the other *unimplanted* edge stays constant. This helps in assigning the edge mode resonances to the edges of the sample.

For the first Co^{2+} implantation, one long and one short edge were irradiated using an ion current of 4.5 pA and a fluence of 5×10^{15} ions/cm^2. For the second run on the same area, a larger ion current of 10 pA and a larger fluence of 5×10^{16} ions/cm^2 were used. Both times, the kinetic ion energy was set to 70 keV. The implanted region was set to a single-pixel line providing a beam width of about 40 nm.

Furthermore, four reference thin-film samples were implanted with Co ions using a conventional broad-beam ion implanter. These reference films were made to determine the magnetic parameters, like saturation magnetization, magnetic anisotropies, and g factor needed as input for the micromagnetic simulations of the strip samples. The kinetic ion energy was set to 35 keV. The same fluences as for the Py strip samples were selected, i.e., 0.5×10^{16}, 1.0×10^{16}, 2.5×10^{16}, and 5.0×10^{16} ions/cm^2, respectively. The fifth reference sample did not undergo any implantation.

III. RESULTS AND DISCUSSION

To assess how the Co implantation will change the magnetic properties, the reference thin-film samples were prepared by broad-beam ion implantation as described above. These films and the unimplanted reference sample were then measured by vibrating-sample magnetometry (not shown) to determine their magnetic moment as a function of irradiation fluence. As higher ion fluences cause a significant sputter effect, we determined the actual film thicknesses from x-ray reflectivity (XRR) measurements to calculate the saturation magnetization $\mu_0 M_s$ properly from the volume of the samples. The effective magnetization $\mu_0 M_{\text{eff}}$ and Landé g factor were determined by vector-network-analyzer (VNA)-FMR measurements. FMR spectra of the thin-film references were recorded at various frequencies between 0 and 30 GHz with the external magnetic field in-plane and out-of-plane configuration as well as angle-dependent, respectively. Each FMR spectrum was fitted with a complex Lorentzian to determine the resonance field H_{res}. Then the resulting angle- and frequency-dependent resonance fields were fitted with the resonance equation to determine the anisotropy fields and g factor.

Using M_s as input, the uniaxial out-of-plane anisotropy constant $K_{2\perp}$ was calculated from the effective magnetization by $\mu_0 M_{\text{eff}} = \mu_0 M_s - 2K_{2\perp}/M_s$. Figure 3 shows the corresponding fluence dependences of the effective magnetization ($\mu_0 M_{\text{eff}}$, blue open circles), saturation magnetization ($\mu_0 M_s$, blue solid circles), and uniaxial out-of-plane anisotropy (red squares), respectively. The actual film thicknesses after implantation as determined from XRR are noted on the top. The fits to the frequency-field dependences of the FMR data of the reference samples reveal that the g factor of 2.11(1) does not change with fluence. With increasing fluence, the saturation magnetization slightly scatters around its bulk value of 1.045 T and finally decreases a little to 0.98 T for 5×10^{16} ions/cm^2. In contrast, the effective magnetization slightly increases by 6%

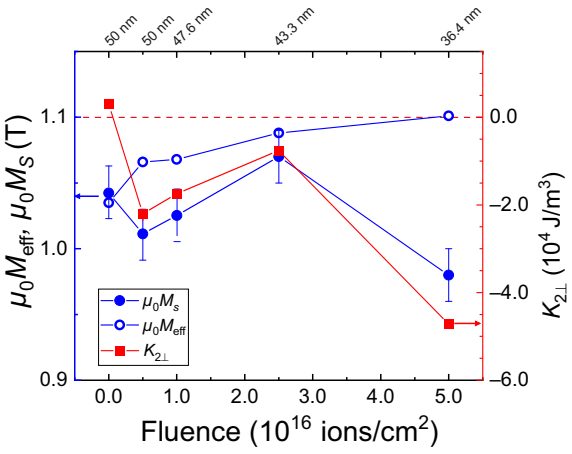

FIG. 3. Co-ion fluence dependence of the saturation magnetization (blue solid circles), effective magnetization (blue open circles), and uniaxial out-of-plane anisotropy (red squares) of the Py reference films. The film thickness determined by XRR is given on the top axis. Arrows denote the y axis to which the plots belong.

with increasing fluence. This is due to a weak uniaxial out-of-plane anisotropy $K_{2\perp}$, which is mainly a surface-related term. It follows the same trend as the magnetization but changes sign once implantation has happened. This is a clear indicator that the ion implantation also influences the surface region and not only the deeper film regions. Hence, we can expect a significant change of the FMR response of the strip sample when the edge is implanted with higher fluences. The parameters were also used as input for the micromagnetic simulations.

A. Transmission electron microscopy and energy-dispersive x-ray spectroscopy cross-section analysis

To visualize the distribution of the Co ions after the Co FIB processing, a thin cross-sectional lamella was prepared by using a standard Ga FIB (Thermo Fisher HELIOS 5 CX). This lamella was then imaged by scanning transmission electron microscopy (STEM) in combination with spectrum imaging analysis based on energy-dispersive x-ray spectroscopy (EDXS) employing a Thermo Fisher Talos F200X TEM operated at an accelerating voltage of 200 kV.

Figure 1(d) shows the superimposed element distribution of the cross-sectional lamella of the Py strip sample, which was taken along the short axis after the second Co^{2+} implantation to increase the total fluence. The position from which the lamella was cut is indicated by the dashed line in Fig. 1(c). Figures 1(e)–(h) depict the corresponding EDXS-based maps of the individual elements Ni, Fe (which together make the Permalloy $Ni_{80}Fe_{20}$), and the implanted Co, respectively. Looking at the distribution of Co, one might think that it is spread all over the strip. However, this apparent Co signal in the unimplanted region is an artifact due to fitting of superimposed peaks. This yields a residual intensity at the Co K_α peak position at 6930 eV, which is located on the low-energy tail of the Fe K_β peak (maximum at 7057 eV). The close-up in Fig. 1(h) clearly shows a bright and dense Co signal close to the strip edge within a region of about 40–50 nm. The edge is rounded due to sputtering effects. This matches the expectation regarding the Co FIB beam diameter. The Co implantation created only a slight intermixing at the Py/Si interface. Likewise, the initial TRIDYN simulations predicted an intermixed zone of 2–5 nm for 70-keV energy. It should be mentioned that the slightly varying Fe and Ni intensities in the Py strip area are caused by variations of the lamella thickness.

B. Ferromagnetic resonance

The microresonator ferromagnetic resonance measurements on the strip samples were performed using a home-built FMR spectrometer employing a homodyne bridge-type detection scheme based on a Marki Microwave IQ-0318 mixer. As a microwave source, a Keysight Technologies model MXG N5183A microwave generator was used. The microresonator is operated in reflection mode using a circulator. The reflected signal is amplified using a low-noise amplifier before feeding it to the in-phase and quadrature (IQ) mixer for rectification. The "LO" input of the mixer is fed from the reference arm of the bridge by the same microwave. A phase shifter in the reference arm allows for separation of the FMR signals in the I and Q channels of the mixer into pure absorption and dispersion signals. The microwave power at the sample was set to -10 dBm $= 100$ μW. To boost the signal-to-noise ratio, lock-in detection is applied by modulating the external magnetic field at a sinusoidal frequency of 78 kHz and a modulation field amplitude of about 1 mT. Using two lock-in amplifiers, the IQ mixer allows for measurement of the field derivatives of the FMR absorption $\partial\chi''/\partial H$ and dispersion $\partial\chi'/\partial H$ signals simultaneously.

Figure 4(b) shows the field-swept FMR absorption spectra of the strip samples for the different implantation states measured at $f = 14.08$ GHz with the magnetic field applied in the magnetically hard direction: the edge-polished sample (blue) and after each of the two Co FIB implantation steps (red and green curves). As it will turn out, applying the field in the hard-axis direction probes spin-wave modes parallel to the long edges of the sample, which are five times longer than the short edges in our case. Thus, the FMR signal is correspondingly five times stronger in the hard-axis direction. That is why only hard-axis measurements are presented here. The effect on the short edges is similar but weaker.

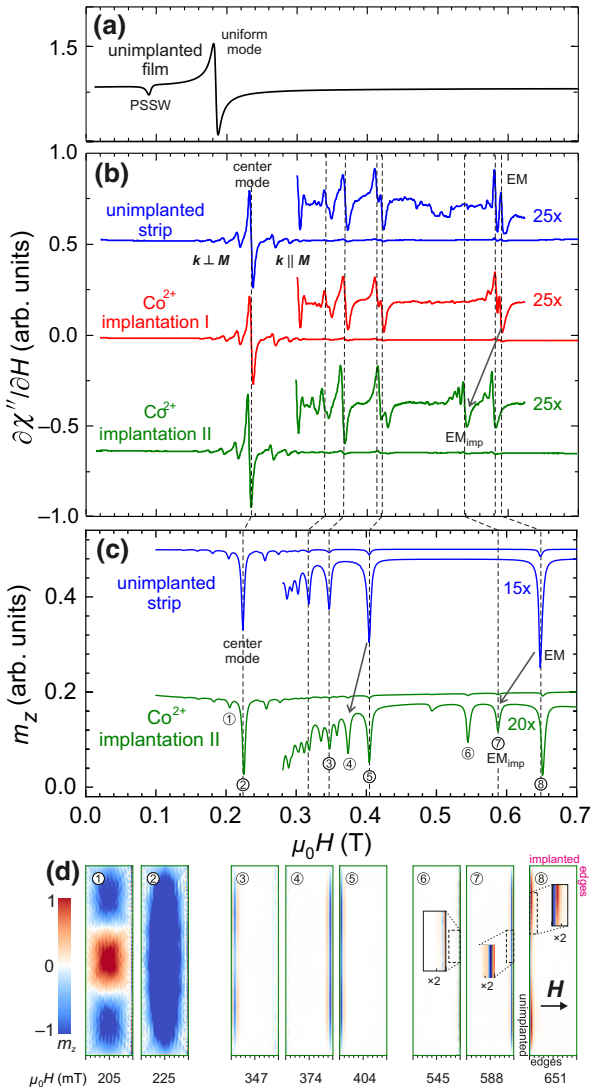

FIG. 4. (a) VNA-FMR spectrum of the unimplanted reference film measured at $f = 14.0$ GHz with in-plane field. (b) Microresonator-FMR spectra of the strip samples measured at $f = 14.080$ GHz with the field applied along the hard axis: blue, unimplanted edge-polished state; red, 40-nm-wide implantation at one short and one long edge of the strip with a Co^{2+} fluence of 0.5×10^{16} ions/cm^2; and green, after a second implantation giving a total Co^{2+} fluence of 5×10^{16} ions/cm^2. (c) Micromagnetic simulations with parameters set according to the measurements of the reference film samples: blue, unimplanted strip; and green, strip implanted with the highest Co^{2+} fluence of 5×10^{16} ions/cm^2. Dashed lines and arrows are guides to the eye marking corresponding resonance modes. (d) Selected mode maps, showing a snapshot of the precession component m_z depicting areas in resonance in blue and red.

The experimental FMR spectra are measured using field modulation; therefore, the line shape resembles the field derivative ($\partial\chi''/\partial H$) of a Lorentzian absorption curve. A multitude of more than 20 resonances is found for the strip samples, with the highest peak around 0.23 T. The very high dynamic range of the microresonator setup allows for detection of even the faintest modes close to 0.6 T. In contrast to that, the FMR spectrum of the unimplanted reference-film sample shown in Fig. 4(a) is much simpler. It just consists of the uniform resonance mode and the first perpendicular standing spin-wave (PSSW) mode only. The uniform mode appears at slightly lower fields compared to the strip's center mode because of the different shape anisotropy field compared to the microstrip sample.

To help in identifying the type and origin of the various resonance modes of the strip samples, micromagnetic simulations using the MUMAX^3 package [32] were performed. For the unimplanted Permalloy strip, a cuboid strip sample was discretized into $512 \times 128 \times 3$ cells. This corresponds to a cell size of $9.5 \times 8 \times 17.7$ nm^3. The magnetic parameters of the Py were taken from the experiments performed on the reference film. As the cross-sectional TEM image in Fig. 1(h) shows, the 40-nm-wide Co-implanted zone at the edge exhibits a curved surface. To accommodate this, the curvature was approximated by two 20-nm-long and 10.6-nm-high steps as sketched in Fig. 1(i). For this, the vertical cell size was reduced to 10.6 nm, corresponding to five vertical layers. The blue boxes mark cells with Permalloy parameters, whereas the red cells use Co-implanted Permalloy parameters as retrieved from the corresponding reference film samples. Only the spin-wave stiffness of the Co-implanted region was set to the Py bulk value of $A = 13$ pJ/m.

The simulated resonance spectra are shown in Fig. 4(c). They depict the m_z component, which corresponds to the absorption signal (no field derivative). The vertical dashed lines mark selected resonances that will be discussed and compared to the experiment in the following. The experimental and simulated spectra match quite nicely up to about 350 mT. There is a slight offset in the resonance field between experiment and simulation. The reason is the simplified geometry in the simulation. In addition to the FMR spectra, the micromagnetic simulations also provide the snapshots of the spatial mappings (i.e., the m_z component) of the resonant modes. For selected resonances, labeled with circled numbers, the mode maps of the implanted strip are given in Fig. 4(d). Areas with blue and red color depict the regions where the magnetic moments precess in resonance.

The main resonance (the one with the highest intensity at around 235 mT in the experiment and 225 mT in the simulation, respectively) arises obviously from the uniform precession of the moments in the central magnetic volume of the strip. This is the so-called center mode; see Fig. 4(d.2). Because of the demagnetizing field, the magnetic moments at and close to the sample's edges face a different local effective magnetic field. Hence, their resonance condition is different from the moments in the center. Therefore, the uniform precession mode, compared to thin-film samples, is confined to the center region of

the structure, where the moments face the same effective field.

At lower and higher resonance fields, further less-intense resonance modes appear. The simulations prove that these modes are localized spin-wave resonance modes emanating from different areas amid the center and the strip rim. The spin-wave modes at fields below the center mode have a wave vector k perpendicular to the magnetization, which can be nicely seen by the pattern in Fig. 4(d.1). Those above have a wave vector parallel to M. The order number of the spin-wave modes increases with the increasing field difference to the center mode. The higher the mode number is, the closer the resonant areas move toward the border of the sample, ultimately reaching it as the edge mode. As the fraction of the sample volume where the resonance of the higher-order modes takes place becomes smaller and smaller, so the intensity of these modes decreases. Such localized modes have been investigated and discussed thoroughly (see e.g. Refs. [23,24,33–38] for further details).

Finally, the resonances at magnetic fields above 500 mT are linked to resonant modes existing only at the very lateral sides of the strip. Therefore, they are called edge modes (EMs). As already mentioned, the moments at the edges face a considerably different effective field than the inner moments due to the demagnetization field. Hence, the energy needed for excitation is lower, which in turn corresponds to a higher resonance field. This is also the explanation why sidewall roughness or sidewall slope of the structure reduce the edge-mode resonance fields [34]. Compared to the center mode, the EMs are very weak because of their very local confinement to the edge of the sample. For example, the area of ion implantation corresponds to only about 4.5% of the total sample area, but the edge mode's localization is even less than that. In the following the focus will be on these edge modes.

In an ideal case of a perfectly symmetric sample, the edge modes of the opposing sample edges would be degenerate, hence, overlapping to a single resonance line. However, due to natural imperfections like the actual shape, roughness, or variation of magnetic properties of both long sides (respectively, both short sides), they are not exactly the same, giving rise to a splitting of the edge modes into slightly different resonance fields [see the blue double-peak structure around 580 mT in Fig. 4(b)]. In fact, one edge might exhibit even more edge modes, because of sample inhomogeneity giving rise to further localization along the edge. As described above, only a narrow (about 40-nm-wide) area along one long and one short edge was implanted with Co ions [see Fig. 1(c)], aiming at modifying exclusively two out of the four edge modes but not the inner localized modes. As the field was applied in the hard-axis direction, i.e., in-plane and perpendicular to the long edges, this means that the FMR essentially probes the influence of the long sample edges, not the short ones.

Figure 4(b) illustrates the influence of the Co^{2+} implantation on the long edge of the strip. In the first run, a modest fluence of 0.5×10^{16} ions/cm^2 was used (red curve), whereas for the second implantation, the fluence was increased to yield in total 5×10^{16} ions/cm^2 (green curve). As expected and simulated in Fig. 4(c), the resonances found at magnetic fields lower than 300 mT do not undergo any significant change, because their active area is localized in the strip's center, i.e., far away from the implanted zone. Therefore, they do not sense any changes in their local magnetic environment. In contrast, one of the two resonances visible at higher magnetic fields (e.g., see the blue curve around 590 mT) is clearly affected. The highest EM first appears at 582 mT in the polished state, at 583 mT after the first low-fluence Co^{2+} implantation, and still at 579 mT after the second one. Just from the FMR spectra it is, therefore, reasonable to assume that this mode is the one located at the unimplanted edge of the strip, as it faces no changes in the magnetic surrounding. In contrast to that, the resonance field of the second EM decreases from 591 to 589 mT after implantation I and finally down to 538 mT after implantation II. This resonance represents obviously the EM associated with the Co^{2+}-implanted long edge (designated as EM_{imp}).

The corresponding simulations in Figs. 4(c) and 4(d) corroborate these findings. For the unimplanted sample (blue curve), the resonances mostly match the positions like in the experimental spectrum, except for the edge mode, which is located at slightly higher fields around 650 mT. As mentioned, the true sample edge geometry differs from the idealized rectangular edge used in the simulation of the unimplanted sample (blue curve). Hence, the EM resonance appears at higher fields than in the experiment. In the simulations of the highest fluence (the green curve, implantation II), one EM (no. 8) stays in position, whereas the other EM (no. 7) is shifted downward by about 60 mT like in the experiment. The mode maps show that the two EMs are located on the opposite long edges. The blue and red contrast for no. 8 appears at the unimplanted edge and is located within 25 nm from the edge. For resonance no. 7 the contrast appears at the implanted edge within 60 nm from the edge.

In addition, two more resonances appear at 490 and 540 mT, which seem to have no counterpart in the experiment. Mode profile no. 6 reveals that they are also edge modes on the implanted side. They are associated with the step-edge profile used for the simulation, i.e., each step creates its own edge mode. In the case of a perfect rectangular edge, there would be only one edge mode. Nevertheless, as the real edge has no steps but is evenly curved, these resonances do not appear in the experimental spectrum.

The resonances around 350–450 mT (experiment) stretch over 150 nm from the edge. Thus, they still face some ion-induced changes in their magnetic surrounding. From the simulation profiles, one can see that they are the

next-higher-order spin-wave modes localized a bit farther away from the edge. The other localized modes below 300 mT are distributed between the center mode and the edge modes and do not show significant changes, as they are far away from the influence of the ion-modified zone. This also means that the modes become symmetric (degenerate) with respect to the centerline of the strip.

IV. CONCLUSION

In conclusion, we have locally modified the magnetism and spin-wave resonances in micrometer-sized Permalloy strips using maskless focused Co-ion-beam implantation. We have achieved a Co-ion-beam diameter of about 40–50 nm. The reduced magnetization in the implanted regions shifts the spin-wave resonances to lower resonance fields, or, in other words, increases their energy. The edge-localized resonances are affected the most, as they are susceptible to the tiniest changes in their magnetic surrounding, i.e., changes in the demagnetization field.

The results are corroborated by micromagnetic simulations. Such direct local *writing* with focused *magnetic* ions is important for various purposes. It facilitates Brillouin-light scattering or magneto-optic Kerr-effect measurements, where otherwise ion-beam-hardened resist masks are very difficult to remove. Moreover, using spatially resolved FIB with magnetic elements to selectively modify the magnetic properties of spin-wave modes, one has an easy handle to control their behavior.

ACKNOWLEDGMENTS

We thank A. Kunz for the TEM specimen preparation and T. Naumann for x-ray reflectivity measurements. Support by the Nanofabrication Facilities Rossendorf (NanoFaRo) and the Structural Characterization Facilities at the IBC is gratefully acknowledged. The funding of TEM Talos by the German Federal Ministry of Education and Research (BMBF, Grant No. 03SF0451) in the framework of HEMCP is acknowledged. The research project was carried out in the framework of the central innovation programme for SMEs (ZIM) under AiF Grant No. ZF4330905AB9. It was supported by the Federal Ministry for Economic Affairs and Energy (BMWi) through the AiF (German Federation of Industrial Research Associations eV) based on a decision taken by the German Bundestag. Some of the authors are part of the FIT4NANO COST Action CA19140.

[1] J. Grollier, D. Querlioz, K. Y. Camsari, K. Everschor-Sitte, S. Fukami, and M. D. Stiles, Neuromorphic spintronics, Nat. Electron. **3**, 360 (2020).

[2] S. Li, W. Kang, Y. Huang, X. Zhang, Y. Zhou, and W. Zhao, Magnetic skyrmion-based artificial neuron device, Nanotechnology **28**, 31LT01 (2017).

[3] T. Blachowicz and A. Ehrmann, Magnetic elements for neuromorphic computing, Molecules **25**, 2550 (2020).

[4] D. Marković, A. Mizrahi, D. Querlioz, and J. Grollier, Physics for neuromorphic computing, Nat. Rev. Phys. **2**, 499 (2020).

[5] C. Chappert, H. Bernas, J. Ferré, V. Kottler, J.-P. Jamet, Y. Chen, E. Cambril, T. Devolder, F. Rousseaux, V. Mathet, and H. Launois, Planar patterned magnetic media obtained by ion irradiation, Science **280**, 1919 (1998).

[6] J. Fassbender, D. Ravelosona, and Y. Samson, Tailoring magnetism by light-ion irradiation, J. Phys. D: Appl. Phys. **37**, R179 (2004).

[7] L. Bruchhaus, P. Mazarov, L. Bischoff, J. Gierak, A. D. Wieck, and H. Hövel, Comparison of technologies for nano device prototyping with a special focus on ion beams: A review, Appl. Phys. Rev. **4**, 011302 (2017).

[8] L. Bischoff, Alloy liquid metal ion sources and their application in mass separated focused ion beams, Ultramicroscopy **103**, 59 (2005).

[9] L. Bischoff, P. Mazarov, L. Bruchhaus, and J. Gierak, Liquid metal alloy ion sources—an alternative for focussed ion beam technology, Appl. Phys. Rev. **3**, 021101 (2016).

[10] P. Mazarov, V. G. Dudnikov, and A. B. Tolstoguzov, Electrohydrodynamic emitters of ion beams, Physics-Uspekhi **63**, 1219 (2020).

[11] F. Machalett, W. Wesch, R. Mühle, and S. Barth, Investigations on liquid alloy ion sources for rare-earth elements, Rev. Sci. Instrum. **69**, 1336 (1998).

[12] P. Siyushev, K. Xia, R. Reuter, M. Jamali, N. Zhao, N. Yang, C. Duan, N. Kukharchyk, A. D. Wieck, R. Kolesov, and J. Wrachtrup, Coherent properties of single rare-earth spin qubits, Nat. Commun. **5**, 3895 (2014).

[13] T. Kornher, K. Xia, R. Kolesov, N. Kukharchyk, R. Reuter, P. Siyushev, R. Stöhr, M. Schreck, H.-W. Becker, B. Villa, A. D. Wieck, and J. Wrachtrup, Production yield of rare-earth ions implanted into an optical crystal, Appl. Phys. Lett. **108**, 053108 (2016).

[14] N. Kukharchyk, R. Neumann, S. Mazarov, P. Bushev, A. D. Wieck, and P. Mazarov, Development of yttrium alloy ion source and its application in nanofabrication, Appl. Phys. A **122**, 1 (2016).

[15] K. Ando, A. Chiba, and H. Tanoue, Uniaxial magnetic anisotropy of submicron MnAs ferromagnets in GaAs semiconductors, Appl. Phys. Lett. **73**, 387 (1998).

[16] J. Fassbender, L. Bischoff, R. Mattheis, and P. Fischer, Magnetic domains and magnetization reversal of ion-induced magnetically patterned Ruderman-Kittel-Kasuya-Yoshida-coupled $Ni_{81}Fe_{19}$/Ru/$Co_{90}Fe_{10}$ films, J. Appl. Phys. **99**, 08G301 (2006).

[17] J. Fassbender, A. Mücklich, K. Potzger, and W. Möller, Mixing and subsequent amorphization of ultrathin $Ni_{81}Fe_{19}$/Ta bilayers by 30 keV Ni implantation, Nucl. Instrum. Methods Phys. Res., Sect. B **248**, 343 (2006).

[18] J. Fassbender and J. McCord, Control of saturation magnetization, anisotropy, and damping due to Ni implantation in thin $Ni_{81}Fe_{19}$ layers, Appl. Phys. Lett. **88**, 252501 (2006).

[19] E. Hesse, L. Bischoff, and J. Teichert, Development of a cobalt liquid alloy ion source, J. Phys. D: Appl. Phys. **27**, 427 (1994).

[20] E. Hesse, W. Driesel, C. Dietzsch, L. Bischoff, and J. Teichert, Shape of a Co–Nd liquid alloy ion source, Jpn. J. Appl. Phys. **35**, 5564 (1996).

[21] R. Narkowicz, D. Suter, and R. Stonies, Planar microresonators for EPR experiments, J. Magn. Reson. **175**, 275 (2005).

[22] R. Narkowicz, D. Suter, and I. Niemeyer, Scaling of sensitivity and efficiency in planar microresonators for electron spin resonance, Rev. Sci. Instrum. **79**, 084702 (2008).

[23] A. Banholzer, R. Narkowicz, C. Hassel, R. Meckenstock, S. Stienen, O. Posth, D. Suter, M. Farle, and J. Lindner, Visualization of spin dynamics in single nanosized magnetic elements, Nanotechnology **22**, 295713 (2011).

[24] C. Schoeppner, K. Wagner, S. Stienen, R. Meckenstock, M. Farle, R. Narkowicz, D. Suter, and J. Lindner, Angular dependent ferromagnetic resonance analysis in a single micron sized cobalt stripe, J. Appl. Phys. **116**, 033913 (2014).

[25] R. Narkowicz and D. Suter, Tuner and radiation shield for planar electron paramagnetic resonance microresonators, Rev. Sci. Instrum. **86**, 024701 (2015).

[26] K. Lenz, R. Narkowicz, K. Wagner, C. F. Reiche, J. Körner, T. Schneider, A. Kákay, H. Schultheiss, U. Weissker, D. Wolf, D. Suter, B. Büchner, J. Fassbender, T. Mühl, and J. Lindner, Magnetization dynamics of an individual single-crystalline Fe-filled carbon nanotube, Small **15**, e1904315 (2019).

[27] Raith GmbH, *Raith VELION FIB-SEM System*, Tech. Rep. (2022), downloaded 2022-03-16, https://raith.com/product/velion/.

[28] L. Bischoff, Application of mass-separated focused ion beams in nano-technology, Nucl. Instrum. Methods Phys. Res., Sect. B **266**, 1846 (2008).

[29] M. Wortmann, A. Ludwig, J. Meijer, D. Reuter, and A. D. Wieck, High-resolution mass spectrometer for liquid metal ion sources, Rev. Sci. Instrum. **84**, 093305 (2013).

[30] L. Bischoff, B. Schmidt, C. Akhmadaliev, and A. Mücklich, Investigation of FIB assisted $CoSi_2$ nanowire growth, Microelectr. Eng. **83**, 800 (2006).

[31] W. Möller, W. Eckstein, and J. Biersack, Tridyn-binary collision simulation of atomic collisions and dynamic composition changes in solids, Comput. Phys. Commun. **51**, 355 (1988).

[32] A. Vansteenkiste, J. Leliaert, M. Dvornik, M. Helsen, F. Garcia-Sanchez, and B. Van Waeyenberge, The design and verification of MuMax3, AIP Adv. **4**, 107133 (2014).

[33] R. D. McMichael and M. D. Stiles, Magnetic normal modes of nanoelements, J. Appl. Phys. **97**, 10J901 (2005).

[34] R. D. McMichael and B. B. Maranville, Edge saturation fields and dynamic edge modes in ideal and nonideal magnetic film edges, Phys. Rev. B **74**, 024424 (2006).

[35] B. B. Maranville, R. D. McMichael, and D. W. Abraham, Variation of thin film edge magnetic properties with patterning process conditions in $Ni_{80}Fe_{20}$ stripes, Appl. Phys. Lett. **90**, 232504 (2007).

[36] H. T. Nembach, J. M. Shaw, T. J. Silva, W. L. Johnson, S. A. Kim, R. D. McMichael, and P. Kabos, Effects of shape distortions and imperfections on mode frequencies and collective linewidths in nanomagnets, Phys. Rev. B **83**, 094427 (2011).

[37] H.-J. Chia, F. Guo, L. M. Belova, and R. D. McMichael, Two-dimensional spectroscopic imaging of individual ferromagnetic nanostripes, Phys. Rev. B **86**, 184406 (2012).

[38] S. Pile, S. Stienen, K. Lenz, R. Narkowicz, S. Wintz, J. Förster, S. Mayr, M. Buchner, M. Weigand, V. Ney, J. Lindner, and A. Ney, Nonstationary spin waves in a single rectangular permalloy microstrip under uniform magnetic excitation, Phys. Rev. B **105**, 094415 (2022).